

Porous Carbon Derived from Petals of Yulan Magnolia Doped with Ni and NiO as Anodes for Lithium Ion Battery

Shouhui Chen*, Yuzhe Zhang, Yanfei Li, Wenbin Liu, Yonghai Song and Li Wang

College of Chemistry and Chemical Engineering, Jiangxi Normal University, 99 Ziyang Road, Nanchang 330022, China

*E-mail: cs2k@sina.com

Received: 2 October 2018 / *Accepted:* 12 November 2018 / *Published:* 5 January 2019

Doping transition metal in biomass-derived carbon is a very common method to preparing anodes for lithium-ion batteries (LIBs). In this study, porous carbon derived from the petals of Yulan magnolia was doped with metallic nickel firstly. Thus, the metallic nickel core in the above prepared precursor was covered by a graphite thin shell, which enabled the core to endure hydrochloric acid etching to some degree. To improve its electrochemical ability as anodes for LIBs, the precursor was oxidized in air at different temperatures from 380 °C to 480 °C. The effects of oxidation temperature to the morphologies, phase, BET surface areas were characterized via TEM, XRD, nitrogen adsorption isotherm, etc. And then the materials were compared as anodes for LIBs. It was found that the material oxidized at 430 °C delivered a discharge capacity of 386.9 mAh g⁻¹ after 100 cycles at 100 mA g⁻¹, which was superior to the electrochemical performance of other composites. The reasons were further elaborated by voltage profile, CV, and XPS.

Keywords: lithium-ion batteries; NiO; biomass-derived carbon; porous material; anodes

1. INTRODUCTION

Nowadays, lithium-ion batteries (LIBs) have become one of the most important energy storage devices for portable electronics and electric vehicles [1-8]. Traditionally, the commercial anode for LIBs is graphite, which delivers a maximum theoretical capacity of 372 mAh g⁻¹ via lithium intercalation reaction. However, extensive research on anodes to date has stretched the mechanisms of lithium intercalation reaction to the lithium conversion reaction and alloying reaction [4-6]. It has been found that the theoretical capacities of transition metal oxides with conversion reactions are several times that of graphite with intercalation-type mechanism. NiO, a kind of transition metal oxides, has been widely

studied for its lithium conversion reaction [8]. To improve the practical capacities of NiO during the prolong discharge/charge cycles, a popular strategy is to fabricate nanostructures with large specific surface area, such as hollow, core-shell, nanosheets, nanowires, and other nanostructures [6-8].

Another strategy is to enhance the electrical conductivity of NiO by preparing composites with other good conductors. For instance, Luo *et al.* prepared C/Ni-NiO nanofibers via electrospinning of polyacrylonitrile [9]. Recently, Huang *et al.* fabricated a cubic nanocomposite containing NiO and carbon as anodes for LIBs by calcining metal-organic frameworks [10]. In these reports, NiO dispersed well in carbon materials. And the carbon materials in the composites acted as a mechanical host to support the large capacity materials, a separating chamber to prevent aggregation of nanoparticles, and an electrical conductor to improve the conductivity of the whole composite [11-13]. However, the relatively expensive cost of raw materials hindered them from wide application.

As an alternative method, natural plants have provided possibilities to the preparation of porous carbon because their tissues are mainly comprised of organic carbon, like lignin, cellulose, hemicellulose, and etc [14,15]. Natural plants have been used to produce charcoal for thousands of years. In the modern industrial society, plants are abundant natural resources used to manufacture porous carbon material to fulfill various industrial demands [16,17]. Carbon derived from plants usually has micropores, mesopores, or macropores. What's more, carbon derived from the same part of a plant can have different pore characteristics via different treatments. Subsequently, our group tried to loading various transition metal oxides on the biomass-derived porous carbon. Many of the prepared materials had show superior electrochemical performances when severed as anodes for LIBs. However, we sometimes found that in the prepared materials, metal would be in company with metal oxides even when pyrolysis in air [18]. In the LIBs' conversion reaction, although few pure transition metals have direct electrochemical contribution to LIBs' capacity instead transition metal oxide, they can still improve the conductivity of the composite [19]. Since metals can be oxidized in air at a relatively high temperature, it is necessary to investigate the oxidation effect in air at the high temperatures to the as-prepared materials containing biomass-derived carbon.

In this study, a precursor of metallic nickel encapsulated in porous carbon was firstly prepared by simply immersing the petals of Yulan magnolia in a nickel-ion aqueous solution, followed by heat treatment in nitrogen atmosphere. Then the precursor was oxidized in air between 380~480 °C to get rid of part of carbon covering on metallic nickel and to oxidize metallic nickel. The effects of heat treatment in air to morphologies, phase changes of nickel, pore characteristic of as-prepared were investigated. And then the as-prepared samples of NiO/Ni-porous carbon were fabricated as anodes for LIBs. We found that a sample oxidized at 430 °C had a stable electrochemical performance. It delivered a discharge capacity of 386.9 mAh g⁻¹ after 100 cycles at 100 mA g⁻¹. Therefore, the petals of Yulan magnolia could be a potential platform to load nickel nanoparticles for the study of energy storage.

2. EXPERIMENTAL

2.1 Materials

Petals of Yulan magnolia were collected from the campus of our university. Nickel chloride hexahydrate was purchased from Sinopharm Chemical Reagent Co., Ltd. Hydrochloric acid was

obtained from Nanchang Xinguang Fine Chemical Plant. Distilled water was provided by Merck Millipore Milli-Q Direct8. Polyvinylidene fluoride (PVDF), carbon black, 1-methyl-2-pyrrolidinone (NMP), copper foil (10 μm thickness), and lithium foil (0.6 mm thickness) were obtained from Shanghai Lefu Chemicals, Shanghai Kaisai Chemicals, Aladdin industrial cooperation, Guangzhou Jiayuan Company, and Tianjin Zhongneng Company, respectively.

2.2 Preparation of Petal-derived porous carbon/Ni composites

Firstly, the petals of Yulan magnolia were cleaned and cut into small pieces. Secondly, 12.0 g of cut fresh petals were directly immersed into 100.0 mL of 0.70 mol L⁻¹ NiCl₂·6H₂O solution for 7 days. After filtered and dried at 60 °C overnight, the petals were placed in a tubular furnace and kept at 900 °C for 4 hours with a ramp rate of 10 °C min⁻¹ in nitrogen atmosphere. Then they were treated with hydrochloric acid (50% (v/v) aqueous, (1+1)) for 2 hours at room temperature, followed with cooling, filtering and drying at 80 °C overnight, and the dried product was named as YNC080. YNC080 further underwent heat treatments for 4 hours in air at different temperatures. According to the temperatures in the heat treatment, 380 °C, 430 °C, 455 °C, and 480 °C, the products were named as YNC380, YNC430, YNC455, and YNC480, respectively. YIC was a control sample prepared by direct pyrolyzing the petals at 900 °C without any other treatment.

2.3 Characterization

The TEM images and the SEM images were scanned by JEOL JEM-2100 and Hitachi S-3400N, respectively. Raman spectra were recorded by Jobin Yvon LabRAM HR. XRD patterns were obtained by Bruker D8 Advanced. Nitrogen adsorption-desorption isotherms were collected by MicrotracBEL BELSORP-mini II. Thermogravimetric analysis was measured by Perkin-Elmer Pyris Diamond.

2.4 Electrochemical measurements

The electrochemical characteristics of the prepared materials were tested as CR2032-type coin cells. The separator was Celegard 2300 film, and the electrolyte was prepared by dissolving 1.0 mol L⁻¹ of LiPF₆ in a non-aqueous solvent (EC/DMC=1/1, v/v). The lithium foil was used as the counter and reference electrode. The round shape working electrode with a diameter of 14.5 mm was prepared via a traditional slurry method. The thickness of slurry on copper foil was fixed at 100 nm, and the mass ratio of electroactive material, PVDF, and carbon black in the slurry was 8:1:1. Except PVDF and carbon black, the mass of electroactive material on each disc electrode was around 1.1 mg cm⁻². The galvanostatic charge-discharge tests were operated on a battery-testing system (Land CT2001A). Cyclic voltammetry curves (CV) and electrochemical impedance spectra (EIS) were recorded by an electrochemical workstation (CHI760E).

3. RESULTS AND DISCUSSION

3.1 Characteristic of Yulan derived porous carbon

Yulan magnolia [20], known as *Magnolia denudata*, blooms in spring with 10~16 cm petals releasing strong pleasant fragrance. In order to elucidate that nickel chloride can disperse in the inner tissues of Yulan's petals, the petals adsorbed nickel salt were first pyrolyzed in nitrogen atmosphere at a very high temperature, 900 °C. Although studies showed that the biomass is full of oxygen functions [14], the pyrolysis temperature in inert atmosphere was too high to generate nickel oxide. To completely encapsulate the prepared metallic nickel in the Yulan-derived porous carbon, the pyrolysis product was further treated with hydrochloric acid to get rid of metallic nickel on the exterior wall of porous carbon, which was easy to expose in the surrounding liquid solution.

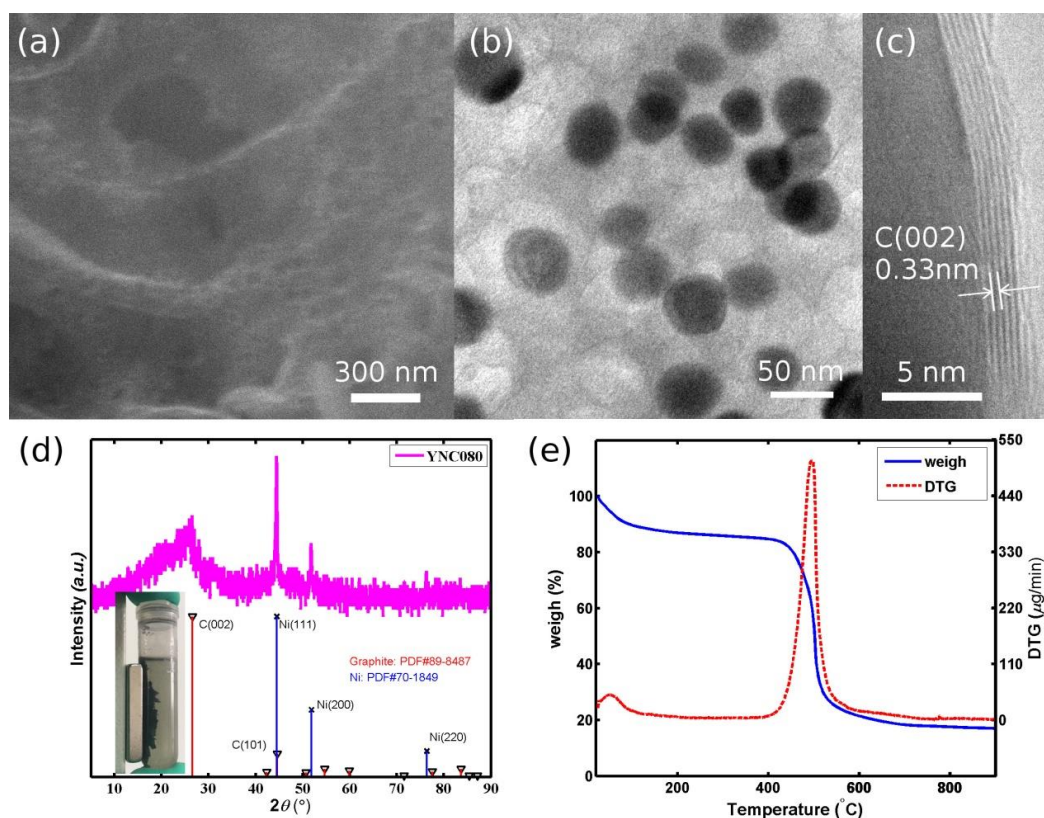


Figure 1. (a) SEM, (b) TEM, and (c) HRTEM images of YNC080; (d) XRD pattern of YNC080, the inset is the magnetic response photo of YNC080 in ethanol; (e) TG-DTG plot of YNC080 in air.

YNC080 has a rougher surface with different size pores (Fig. 1a). TEM image (Fig. 1b) showed the existence of mesopore, which was indicated by the white color in the images, with nickel nanoparticles in the dark color and carbon materials in gray color. The dark spheres in the sample (Fig. 1b) were of core-shell structure with a diameter of around 50 nm, in which the core was metallic nickel and the shell was graphite. HRTEM image (Fig. 1c) also showed that graphite shell had few layers, which might be the result of the catalysis of nickel salts in a certain high temperature. XRD pattern of YNC080 also proved the existence of metallic nickel in YNC080 (Fig. 1d), which was consistent with the

magnetic response of dispersed YNC080 in ethanol solution (inset in Fig. 1d). It should be noted that the Ni nanoparticles remained in YNC080 after acid etching, which might be attributed to the protection function from graphite layer covered on it. Although the graphite shell was generated by the catalysis effect of nickel salt, the broad XRD peak of YNC080 at $\sim 25^\circ$, still indicated that the most of the plant tissues were just carbonized instead of graphitized by direct pyrolyzing natural tissues [21]. Hence, Ni salts can be well dispersed in the interior tissues of Yulan petals, not just the exterior wall of the tissues. And YNC080 was a composite containing nickel core with graphite shell, which was the catalysis product.

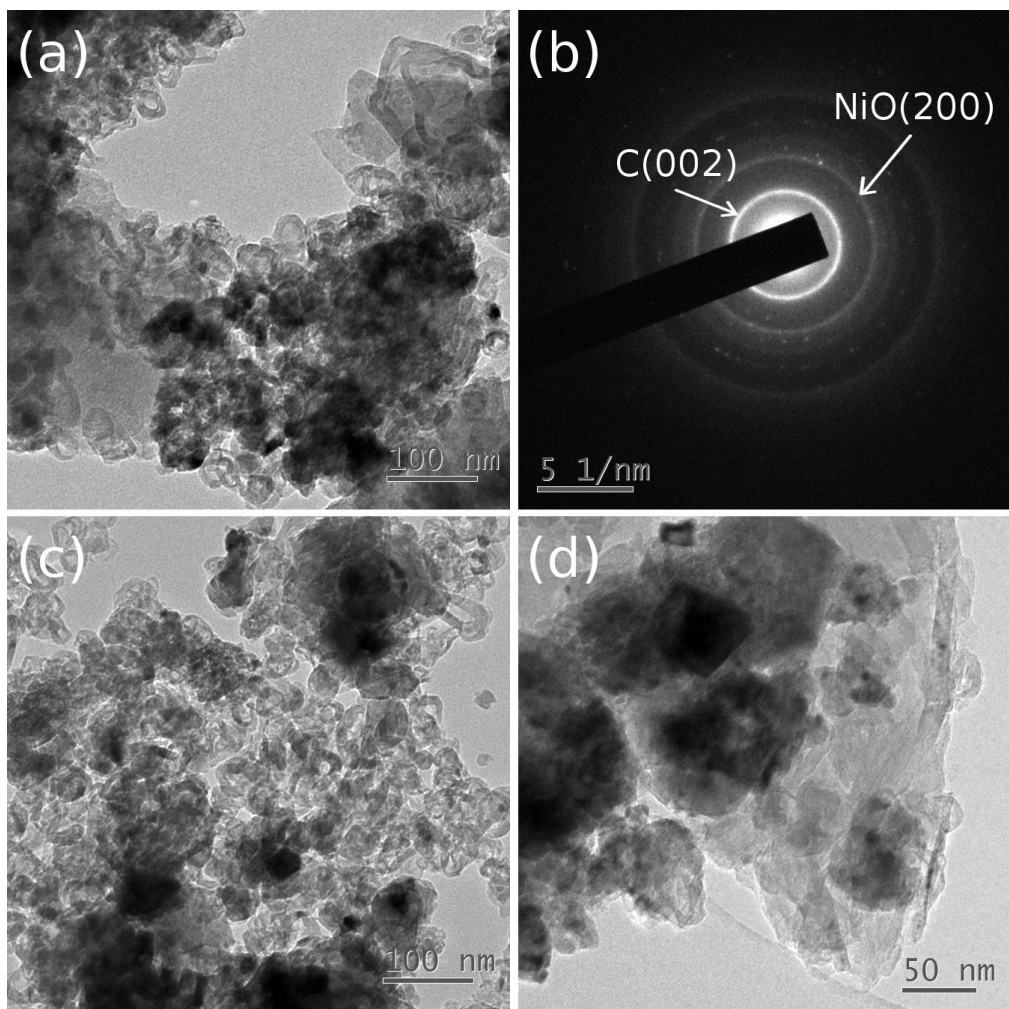


Figure 2. TEM images of (a) YNC430, (c) YNC455, and (d) YNC480; (b) the SAED pattern of YNC430.

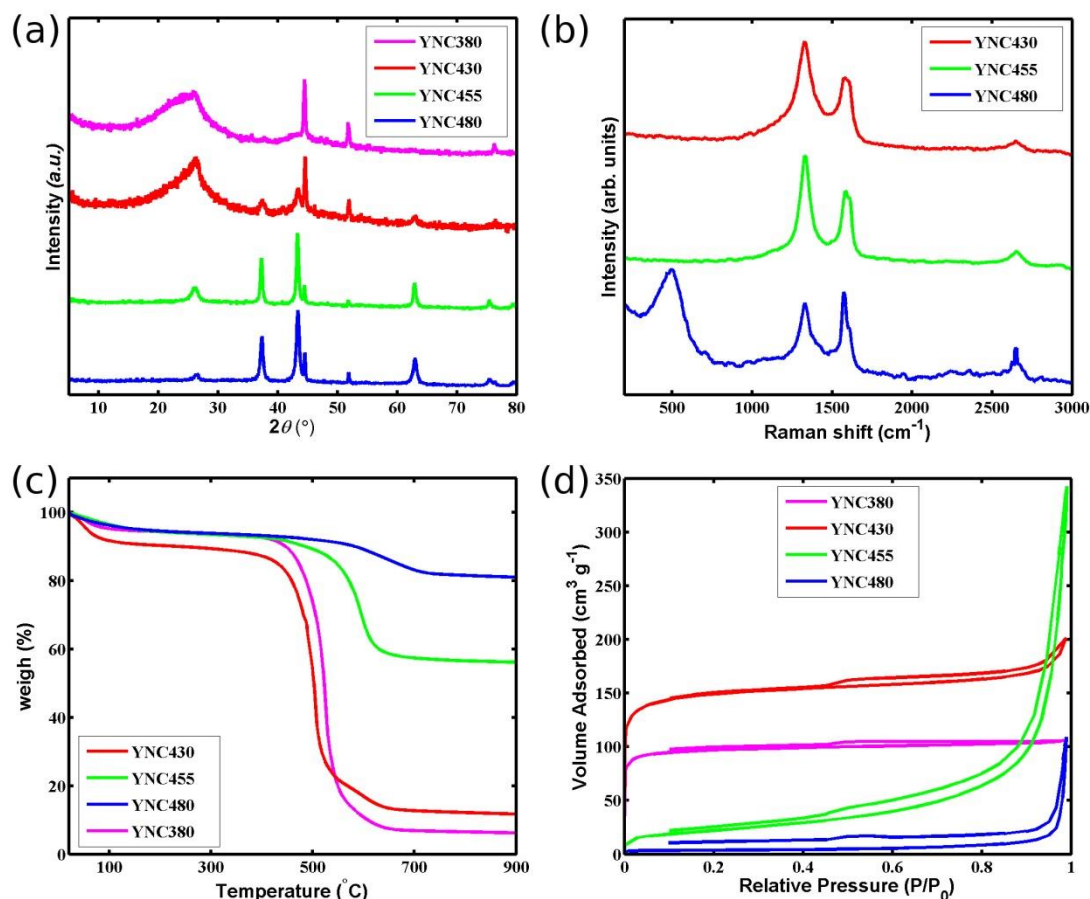


Figure 3. (a) The XRD patterns, (c) TG-DTG plot in air, and (d) nitrogen adsorption-desorption curves of YNC380, YNC430, YNC455, and YNC480; (b) Raman spectra of YNC430, YNC455, and YNC480.

Since metallic nickel has little contribution to the capacity of anode for LIBs, oxidizing nickel to nickel oxide should improve the capacity of anodes. According to TGA plot in Fig. 1e, the temperature range between 380 °C and 480 °C was selected to oxidize metallic Ni encapsulated in Yulan-derived carbon. For instance, after calcined at 430 °C, the spherical graphite shell (Fig. 2a) can be obviously found in the YNC430, with nickel nanoparticles well dispersed in YNC430. Besides, the diffraction rings in SAED pattern (Fig. 2b) distinctively showed (200) plane of NiO and (002) plane of graphite [22-24]. SAED results together with the HRTEM images, demonstrates polycrystalline NiO with graphite in sample YNC430. After calcined at 455 °C, the spherical shell in YNC455 got distorted and even broken. Calcined at a even more higher temperature (480 °C), the graphite ribbons can be found in YNC480 instead of spherical shell. It was suggested that the graphite protective shell could be destroyed at a relatively high temperature in air.

As shown in Fig. 3a, when the temperature was still at 380 °C, there were no apparent XRD peaks related to NiO generated in YNC380. Although metallic nickel would be oxidized to NiO when temperature is above 300 °C [22,25], the experiment condition of 4 hours at 380 °C in air can't be used to easily oxidize the metallic nickel in YNC380, indicating that Ni nanoparticles could be well protected by the surrounding Yulan-derived carbon. In order to generate NiO quickly, a high temperature was

adapted to consume the outside protective Yulan-derived carbon. When temperature raised up to 430 °C, the XRD peak of carbon material remained broad, however, the weak XRD peaks of NiO indicated the oxidation of metallic nickel might come from the partial destroy of carbon protect layer on it. Compared with the signals of YNC430, the relative intensity of the metallic nickel XRD peak in YNC455 decreased, while that of the NiO peak increased when the temperature was 455 °C, demonstrating that the conversion of metallic nickel to NiO. And the XRD peak of carbon material in YNC455 was distinctively less and sharper than that in YNC430. When the temperature was up to 480 °C, the relative intense of carbon material in YNC480 further weakened, indicating the depletion of most of the surrounding carbonized material.

The effect of oxidation temperature can also be referred to Raman spectra (Fig. 3b). Both YNC430 and YNC455 had characteristic peaks of carbon material at $\sim 1325\text{ cm}^{-1}$ and $\sim 1580\text{ cm}^{-1}$, presenting the D band and the G band of carbon materials. The ratios of I_G to I_D were about 0.70, indicating the content of amorphous carbon was larger than that of graphite. The Raman peak centered at 2650 cm^{-1} was the 2D band of graphite [26], resulting from the few lays of graphite covered on the nickel particle (Fig. 2). When the temperature increased to 480 °C, the ratio of I_G to I_D increased to 1.14, and the 2D band of graphite was much sharper, which meant the increase of graphite content. Moreover, the high calcination temperature not only depleted amorphous carbon in the YNC480, but also made the generated NiO exposed out, as the Raman peak located at 495 cm^{-1} indicating the NiO stretching mode [27]. It confirmed that the selected temperatures in air could be used to adjust the phase in YNC080.

Fig. 3c is the TGA plot of Yulan derived porous carbon in air atmosphere. As shown in the figure, the weight lost below 100 °C was contributed to the evaporation of water in the compounds. And then, in the temperature range of 350 °C to 480 °C, the weight lost were mainly caused by the oxidation of carbon materials. In order to simplify the following discussion in the section of LIBs performance, the components in the YNC series material were simplified as carbon and NiO. After calculation, it was found that the contents of NiO in YNC380, YNC430, YNC455, and YNC480 were 6.9%, 13.5%, 60.0%, and 86.3%, respectively. The calculation of contents would be helpful to estimate the initial capacity of the corresponding anodes.

Table 1. Comparison of pore characteristic of YNC380, YNC430, YNC455, and YNC480.

	YNC380	YNC430	YNC455	YNC480
BET surface area ($\text{m}^2\text{ g}^{-1}$)	319	498	80	12.6
Total pore volume ($\text{cm}^3\text{ g}^{-1}$)	0.164	0.312	0.518	0.168
Mean pore size (nm)	2.0	2.5	25.9	53.3

The pore characteristics of YNC380, YNC430, YNC455, and YNC480 were measured by nitrogen adsorption-desorption curves. As shown in Fig. 3d and Table. 1, YNC380 had features of both microporous and mesoporous [21]. Its mean pore size was 2.0 nm, which was the smallest among the four compounds. Although YNC430 had a similar isotherm with YNC380 as well as the mean pore size of $\sim 2\text{ nm}$, its BET surface area is the biggest among the four compounds, $498\text{ m}^2\text{ g}^{-1}$. When the temperature kept increasing, the isotherms of YNC455 and YNC480 showed only mesoporous

characteristic [28]. YNC455 had the biggest total pore volume and YNC480 had the biggest mean pore size. That the mean pore size of the four compounds increased with the temperature may be attributed to the increase of NiO pore size. And that both the BET surface area and total pore volume increased firstly and then decreased may be attributed to the change of microporous carbon and mesoporous NiO in the composites. It could be concluded that when the oxidation temperature raised from 380 °C to 480 °C, the microporous structures from biomass-derived carbon increased firstly, and then decreased. While the pore related to nickel turned from microporous to mesoporous, and to macroporous.

3.2 Electrochemical behaviors of Yulan derived porous carbon

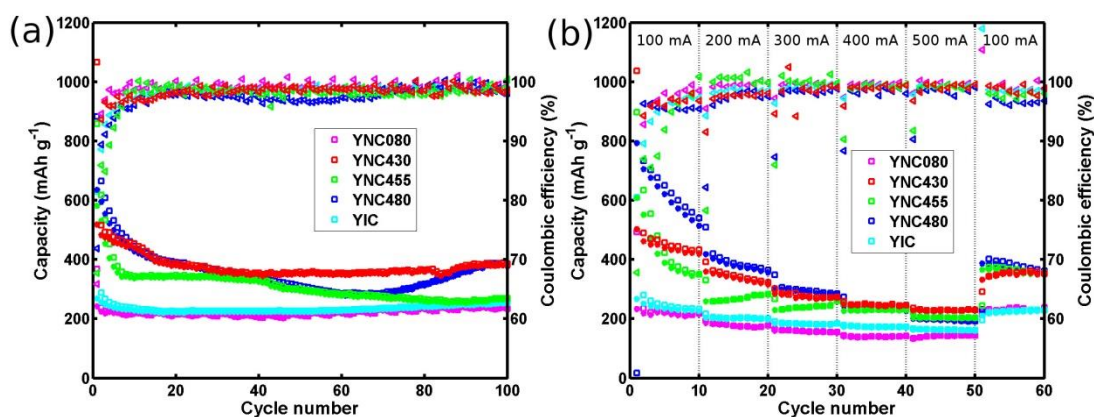


Figure 4. (a) Cycle performance and the corresponding Coulombic efficiency of YIC, YNC080, YNC430, YNC455, and YNC480 at 100 mA g⁻¹; (b) Rate capability at current densities range from 100 to 500 mA g⁻¹.

To compare the electrochemical behaviors of these materials, they were tested as the anodes for LIBs in the range of 0.01~3.00 V at first. As shown in Fig. 4a, when the current was 100 mA g⁻¹, all of the reversible capacity of YNC430, YNC455, and YNC480 declined quickly at the first dozen of discharge/charge cycles. and then the changing trend of their capacities ran diverse. During the following cycles, the reverse capacity of YNC430 turned to stable, while that of YNC455 was still on the decline, and that of YNC480 presented an obvious undulation. At last, YNC430, YNC455, and YNC480 delivered a discharge capacity of 386.9 mAh g⁻¹, 275.6 mAh g⁻¹, 385.8 mAh g⁻¹ with Coulombic efficiencies of ~99%, respectively. The rate capability test was shown in Fig. 4b. In the figure, it was found that YNC430 delivered 433.0 mAh g⁻¹, 322.4 mAh g⁻¹, 272.9 mAh g⁻¹, 246.6 mAh g⁻¹, and 230.0 mAh g⁻¹ at the currents density of 100 mA g⁻¹, 200 mA g⁻¹, 300 mA g⁻¹, 400 mA g⁻¹, 500 mA g⁻¹, respectively. The capability of YNC430 was between that of YNC455 and that of YNC480 when the current density was not more than 300 mA g⁻¹, and that of YNC430 was larger than that of YNC455 and that of YNC480 when the current density was between 400 and 500 mA g⁻¹. As control samples, both YNC080 and YIC had similar reversible capacities in the cycle performance and the rate performance (Fig. 4). That the capacity of YNC080 was slightly lower than that of YIC might because the doped metallic nickel in YNC080 had none contribution to the capacity of the whole composites. The above results were not consisted with the prediction suggested by the TGA plot (Fig. 3c), which showed

different NiO contents in the composites and the corresponding theoretic capacity delivered by the composites.

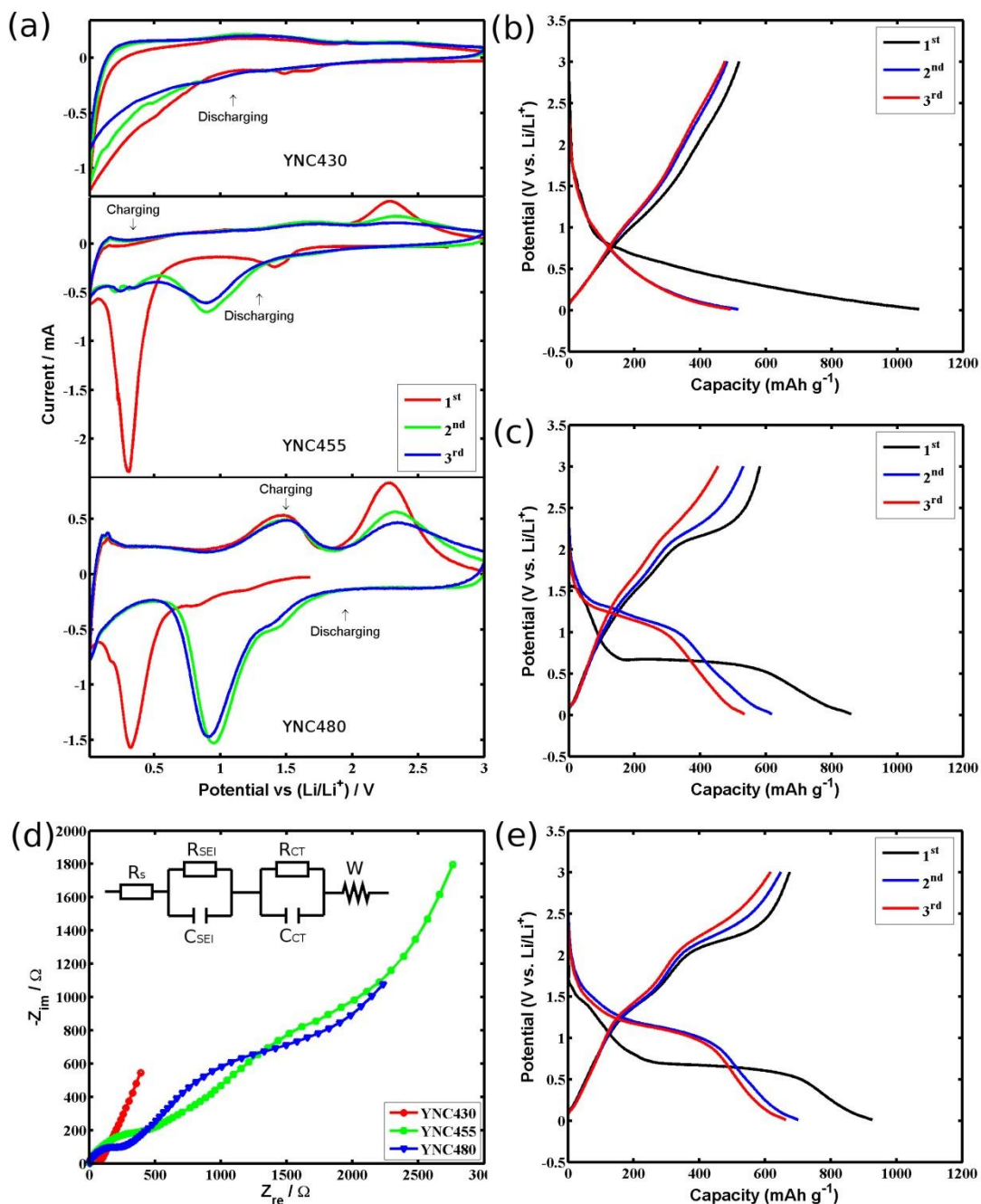
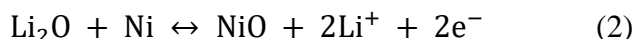
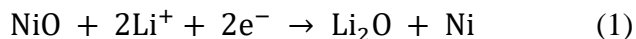


Figure 5. (a) Cyclic voltammograms of YNC430, YNC455, and YNC480 between 0.01 and 3.00 V with a scan rate of 0.2 mV s⁻¹; Galvanostatic potential profiles of (b) YNC430, (c) YNC455, and (e) YNC480 in the first 3 cycles at 100 mA g⁻¹; (d) The electrochemical impedance spectra of YNC430, YNC455, and YNC480.

To find the difference between the practical capacity and the theoretic capacity, the first three cyclic voltammeter (CV) curves of YNC430, YNC455, and YNC480 at a scan rate of 50 mV s⁻¹ between 0.01 V and 3.00 V was compared (Fig. 5a). According to the lithium storage mechanism of NiO, the

electrochemical reaction of NiO during the charging/discharging process can be expressed as the following [29]:



As for YNC480, in the first cathodic scan, the tiny peaks between 0.80 and 1.50 V were the result of the formation of solid electrolyte interface (SEI) film and the partial reversible generation of polymeric gel-like layer [30-32]. And the peak at 0.50 V was related to the reduction of NiO to metallic Ni and the formation of Li₂O. Then the peak shifted positively from 0.50 V to ~0.93 V in the subsequent cathodic scans, indicating irreversible structure change during the charge/discharge cycles [30-33]. In the anodic scans, the two peaks at ~1.50 V and ~2.30 V were ascribed to the decomposition of SEI film and the oxidation of metallic Ni to NiO, respectively. YNC455 had a relatively obvious reduction peak of NiO at 0.30 V and oxidation peak of Ni at 2.28 V at the first cycle. And then the reduction peak shifted and the redox peaks suppressed in the following cycles. Because the content of NiO in YNC430 was insufficient, the redox peaks related to NiO and Ni were not easy to be found in the figure. And it presented an evident intercalation type of mechanism of carbon materials.

The galvanostatic potential profiles of YNC430, YNC455, and YNC480 in the first 3 cycles at 100 mA g⁻¹ were shown in Fig. 5b-d, respectively. YNC430 had the typical galvanostatic potential profile of carbon materials (5b) as well as the CV's suggestion (Fig. 5a) [34]. Both YNC455 (Fig. 5c) and YNC480 (Fig. 5e) had similar galvanostatic potential profiles. According to the discharge curves, the plateaus at ~0.65 V in the first cycle was related to the reduction of NiO [31,35,36]. And then they were shifted to ~1.1 V in the following cycles [31,35,36], which coincided with the result of CV. Furthermore, it was shown that the charge capacity and discharge capacity of YNC480 at the initial cycles were more stable and larger than that of YNC455. Both CV curves and the galvanostatic potential profiles showed that the main lithium storage mechanisms of the three anodes were different, which were related to the contents of NiO and C in the anodes.

Table 2. Comparison of the fitted data of electrochemical impedance data of YNC430, YNC455, and YNC480 after 100 cycles at 100 mA g⁻¹ via a equivalent circuit (R_s(R_{SEI}C_{SEI})(R_{CT}C_{CT})W).

	YNC430	YNC455	YNC480
R _s (Ω)	4.65 ± 0.20	3.11 ± 0.32	3.63 ± 0.34
R _{SEI} (Ω)	13.20 ± 0.71	83.79 ± 8.69	39.81 ± 5.55
C _{SEI} (μF)	2.44 ± 0.16	1.87 ± 0.12	1.94 ± 0.16
R _{CT} (Ω)	38.79 ± 1.75	376.80 ± 23.75	190.50 ± 12.62
C _{CT} (μF)	35.71 ± 3.10	10.00 ± 1.10	7.53 ± 0.95
W (mΩ)	6.99 ± 0.20	0.90 ± 0.04	1.06 ± 0.04

After cycling at 100 mA g⁻¹ for 100 times, the batteries were further tested by electrochemical impedance spectrum (EIS) [37,38]. And the EIS data were further fitted by a equivalent circuit, R_s(R_{SEI}C_{SEI})(R_{CT}C_{CT})W. According to the fitted data (Fig. 5e and Table 2), it was found that both the resistance of Li⁺ through the SEI film (R_{SEI}) and the charge-transfer resistance on the interface (R_{CT}) was

increased in the turn of YNC430, YNC480, and YNC455, while the Warburg resistance (W) was increased in a reverse turn. It was supposed that an intact protective graphite shell covered on the NiO/Ni core could have functions to facilitate the charge transfer, Li^+ migration and diffusion. When the protective shell was broken, the above functions could be weakened. However, when the shell was thoroughly destroyed, the uncovered core might reinforce the above ability to some degree.

To further obtain the information of YNC430 on its electrochemical behavior, the electronic states of elements on the surface of YNC430 were obtained by XPS. The XPS spectrum (Fig. 6a) revealed that the main elements in YNC430 were C, O, and Ni [39,40]. The high resolution spectrum of Ni 2p (Fig. 6b) can be fitted into two main peaks, Ni 2p_{1/2}, Ni 2p_{3/2}, and their corresponding satellite peaks at the binding energy of 855.8 eV, 873.6 eV, 861.3 eV, and 879.6 eV, respectively, which were the typical Ni-O bonds in NiO [41,42]. A tiny peak at 853.4 eV was corresponding to metallic Ni [43,44]. Ni-O bond could also be found at the binding energy at 529.2 eV in Fig. 6c [41,44,45]. The spectrum of C 1s (Fig. 6d) can be fitted into peaks related to C-C, C-O-C, and O-C=O bonds at the binding energy of 284.4 eV, 285.2 eV, and 288.8 eV, respectively [43]. Since the presence of metallic Ni existed in YNC430 as well as NiO (Fig. 3a), we think the metallic Ni had been covered by a NiO layer, and the Ni nanoparticles were embedded deeply in the carbon material because the composite underwent 2 hours of high concentration hydrochloric acid treatment and still keep magnetic response.

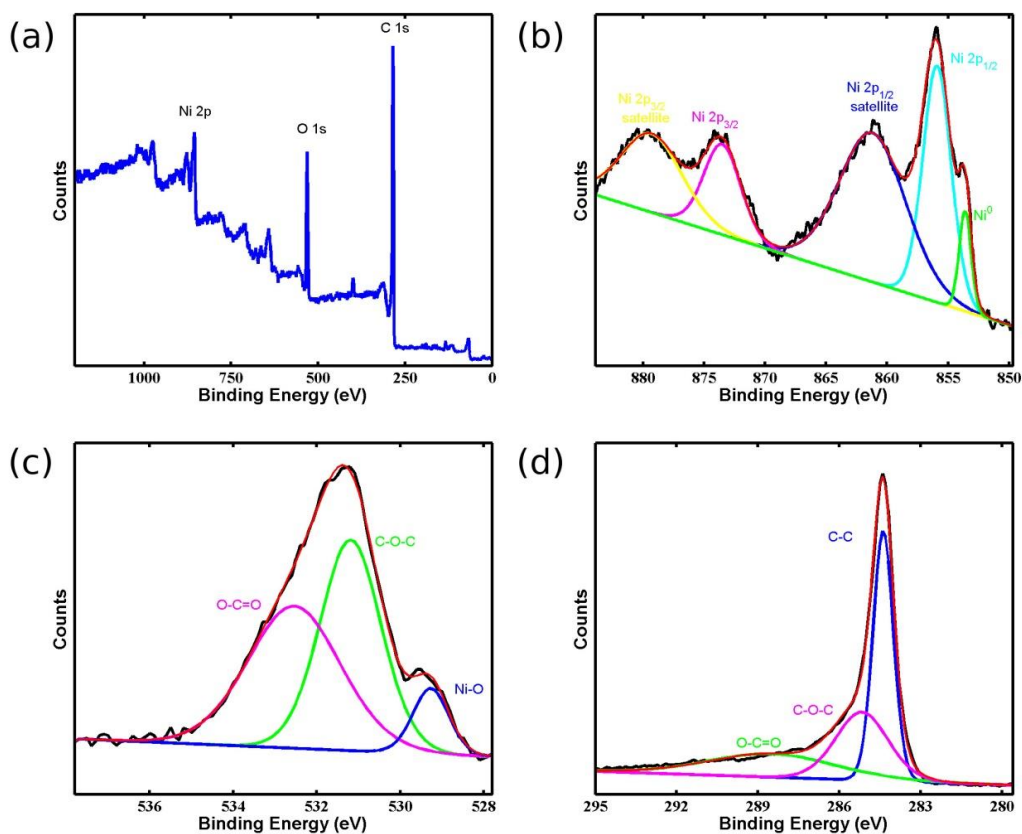


Figure 6. The XPS analysis of YNC430 in (a) full-spectrum, (b) Ni2p, (c) O1s, and (d) C1s.

Graphitizing carbon materials at temperature beyond 2000 °C, using porogens (KOH, ZnCl₂, etc) to increase the specific surface area, doping with heteroatoms or transition metal oxides have been used to improve the specific capacity of biomass-derived anodes for LIBs (Table 3). YNC430 could deliver a specific capacity which was comparable to those of anodes in the table. In this work, which YNC430 had a better electrochemical performance than the other Yulan-derived anodes for LIBs might be ascribed to the following: 1. There was NiO nanoparticles doped in the biomass-derived carbon, which could enhance the capacity of the whole material. 2. YNC430 had features of both microporous and mesoporous, and it had the biggest BET surface area in the four materials, which facilitated the infiltration of electrolyte, and correspondingly, the ions and charge transfer. 3. The NiO nanoparticles doped in YNC430 were protected by a graphite shell, strengthening the charge transfer. 4. There was still a certain metallic Ni in YNC430, which would facilitate the electrical conductivity.

Table 3. Comparison of the specific capacity between YNC430 and other biomass-derived anodes in LIBs.

Materials	Biomass	Pyrolysis		Capacity (mAh g ⁻¹)	Current Density	Reference
		Temperature	Other chemicals			
YNC430	Yulan petals	900 °C	NiCl ₂	387	0.27C	This work
NC-700-I	peanut shell	700 °C	melamine	350	0.2C	[46]
CA-TiO ₂	corn stalks	800 °C	ZnCl ₂ , FeCl ₃ and butyl titanate	203	1C	[47]
BDC-2800	bean-dreg	2100 °C	\	396	0.1C	[48]
BDC-Z	bean-dreg	2100 °C	ZnCl ₂	605	0.1C	[48]
BDC-K	bean-dreg	2100 °C	KOH	748	0.1C	[48]
FCCE	fungus	900 °C	Co(NO ₃) ₂	425	0.1C	[49]
active carbon	rice straw	550 °C	\	250	0.1C	[50]
1100CST	mushroom	1100 °C	\	260	0.2C	[51]
active carbon	rice husk	800 °C	KOH	~400	0.2C	[52]

4. CONCLUSIONS

In summary, pyrolysis of Ni encapsulated in Yulan petal-derived carbon in air at different temperatures was compared. The oxidation of both nickel and carbon, and the corresponding effects of them to phase change, morphology change, the pore characteristic, and the electrochemical performance were investigated. It was found that both the carbon coating on YNC430 and the metallic nickel in it facilitate the charge transfer, Li⁺ migration and diffusion. Correspondingly, YNC430's electrochemical performance was better than those of other Ni-Yulan petal derived materials.

ACKNOWLEDGEMENTS

This work was financially supported by National Natural Science Foundation of China (21465014 and 21465015), and Scientific Research Foundation of Education Commission of Jiangxi Province (GJJ160288).

References

1. L. Yin, Y. J. Gao, I. Jeon, H. Yang, J.-P. Kim, S. Y. Jeong, C. R. Cho, *Chem. Eng. J.*, 356 (2019) 60.
2. P. Santhoshkumar, K. Prasanna, Y. N. Jo, I. N. Sivagami, S. H. Kang, C. W. Lee, *J. Alloy. Compd.*, 771 (2019) 555.
3. M.-L. C. Piedboeuf, A. F. Léonard, G. Reichenauer, C. Balzer, N. Job, *Micropor. Mesopor. Mat.*, 275 (2019) 278.
4. L. Shi, Y. Li, F. Zeng, S. Ran, C. Dong, S.-Y. Leu, S. T. Boles, K. H. Lam, *Chem. Eng. J.*, 356 (2019) 107.
5. K. Wang, S. Pei, Z. He, L.-a. Huang, S. Zhu, J. Guo, H. Shao, J. Wang, *Chem. Eng. J.*, 356 (2019) 272.
6. A. Jain, B. J. Paul, S. Kim, V. K. Jain, J. Kim, A. K. Rai, *J. Alloy. Compd.*, 772 (2019) 72.
7. Y. Wang, L. Chen, H. Liu, Z. Xiong, L. Zhao, S. Liu, C. Huang, Y. Zhao, *Chem. Eng. J.*, 356 (2019) 746.
8. X. Wu, S. Li, Y. Xu, B. Wang, J. Liu, M. Yu, *Chem. Eng. J.*, 356 (2019) 245.
9. C. Luo, W. Lu, Y. Li, Y. Feng, W. Feng, Y. Zhao, X. Yuan, *Appl. Phys. A-Mater.*, 113 (2013) 683.
10. G. Huang, D. Yin, F. Zhang, Q. Li, L. Wang, *Inorg. Chem.*, 56 (2017) 9794.
11. T.-T. Shan, S. Xin, Y. You, H.-P. Cong, S.-H. Yu, A. Manthiram, *Angew. Chem. Int. Edit.*, 55 (2016) 12783.
12. Y. Yang, B. Wang, J. Zhu, J. Zhou, Z. Xu, L. Fan, J. Zhu, R. Podila, A. M. Rao, B. Lu, *ACS Nano*, 10 (2016) 5516.
13. J. Zhu, T. Wang, F. Fan, L. Mei, B. Lu, *ACS Nano*, 10 (2016) 8243.
14. W.-J. Liu, W.-W. Li, H. Jiang, H.-Q. Yu, *Chem. Rev.*, 117 (2017) 6367.
15. F. Chen, A. S. Gong, M. Zhu, G. Chen, S. D. Lacey, F. Jiang, Y. Li, Y. Wang, J. Dai, Y. Yao, J. Song, B. Liu, K. Fu, S. Das, L. Hu, *ACS Nano*, 11 (2017) 4275.
16. X. Zhou, F. Chen, T. Bai, B. Long, Q. Liao, Y. Ren, J. Yang, *Green Chem.*, 18 (2016) 2078.
17. L. Wang, Y. Zheng, Q. Zhang, L. Zuo, S. Chen, S. Chen, H. Hou, Y. Song, *RSC Adv.*, 4 (2014) 51072.
18. R. Zhou, Y. Chen, Y. Fu, Y. Li, S. Chen, Y. Song, L. Wang, *Ionics*, 24 (2018) 1321.
19. M. V. Reddy, G. V. Subba Rao, B. V. R. Chowdari, *Chem. Rev.*, 113 (2013) 5364.
20. H. Yoon, *Food Sci. Biotechnol.*, 23 (2014) 1715.
21. M. Sevilla, G. A. Ferrero, A. B. Fuertes, *Chem. Mater.*, 29 (2017) 6900.
22. H. Du, C. Zhou, X. Xie, H. Li, W. Qi, Y. Wu, T. Liu, *Int. J. Hydrogen Energ.*, 42 (2017) 15236.
23. G. Li, Y. Li, J. Chen, P. Zhao, D. Li, Y. Dong, L. Zhang, *Electrochim. Acta*, 245 (2017) 941.
24. A. Khalil, B. S. Lalia, R. Hashaikh, *J. Mater. Sci.*, 51 (2016) 6624.
25. J. Liang, Y.-Z. Wang, C.-C. Wang, S.-Y. Lu, *J. Mater. Chem. A*, 4 (2016) 9797.
26. S.-M. Yoon, W. M. Choi, H. Baik, H.-J. Shin, I. Song, M.-S. Kwon, J. J. Bae, H. Kim, Y. H. Lee, J.-Y. Choi, *ACS Nano*, 6 (2012) 6803.
27. M. E. Plonska-Brzezinska, D. M. Brus, A. Molina-Ontoria, L. Echegoyen, *RSC Adv.*, 3 (2013) 25891.
28. L. Yu, J. Liu, X. Xu, L. Zhang, R. Hu, J. Liu, L. Yang, M. Zhu, *ACS Appl. Mater. Inter.*, 9 (2017) 2516.
29. Y. Feng, H. Zhang, W. Li, L. Fang, Y. Wang, *J. Power Sources*, 301 (2016) 78.
30. C. Wang, Y. Zhao, D. Su, C. Ding, L. Wang, D. Yan, J. Li, H. Jin, *Electrochim. Acta*, 231 (2017) 272.
31. F. Zheng, S. Xu, Y. Zhang, *J. Mater. Sci. -Mater. El*, 27 (2016) 3576.
32. Q. Li, G. Huang, D. Yin, Y. Wu, L. Wang, *Part. Part. Syst. Char.*, 33 (2016) 764.
33. X. Ma, N. Wang, Y. Qian, Z. Bai, *Mater. Lett.*, 168 (2016) 5.
34. H. Jiang, H. Zhang, Y. Fu, S. Guo, Y. Hu, L. Zhang, Y. Liu, H. Liu, C. Li, *ACS Nano*, 10 (2016) 1648.

35. X. Zhu, B. Luo, T. Butburee, J. Zhu, S. Han, L. Wang, *Micropor. Mesopor. Mater.*, 238 (2017) 78.
36. H. Xu, M. Zeng, J. Li, X. Tong, *RSC Adv.*, 5 (2015) 91493.
37. V. A. Agubra, L. Zuniga, D. Flores, H. Campos, J. Villarreal, M. Alcoutlabi, *Electrochim. Acta*, 224 (2017) 608.
38. R. Verrelli, J. Hassoun, *Chemelectrochem*, 2 (2015) 988.
39. J. Wu, W.-J. Yin, W.-W. Liu, P. Guo, G. Liu, X. Liu, D. Geng, W.-M. Lau, H. Liu, L.-M. Liu, *J. Mater. Chem. A*, 4 (2016) 10940.
40. Y. Li, X. Li, Z. Wang, H. Guo, T. Li, *Ceram. Int.*, 42 (2016) 14565.
41. S. Wang, W. Li, L. Xin, M. Wu, W. Sun, X. Lou, *Chem. Eng. J.*, 321 (2017) 546.
42. H. Liu, X. Wang, H. Xu, W. Yu, X. Dong, Y. Yang, H. Zhang, J. Wang, *Dalton T.*, 46 (2017) 11031.
43. Z.-Y. Luo, S.-S. Lyu, Y.-X. Fu, Y. Heng, D.-C. Mo, *Appl. Surf. Sci.*, 409 (2017) 431.
44. M. M. Gomaa, G. R. Yazdi, S. Schmidt, M. Boshta, V. Khranovskyy, F. Eriksson, B. S. Farag, M. B. S. Osman, R. Yakimova, *Mat. Sci. Semicon. Proc.*, 64 (2017) 32.
45. Y. Hanifehpour, A. Morsali, B. Mirtamizdoust, S. W. Joo, B. Soltani, *Ultrason. Sonochem.*, 37 (2017) 430.
46. L. Liu, L. Yang, P. Wang, C.-Y. Wang, J. Cheng, G. Zhang, J.-J. Gu, F.-F. Cao, *Int. J. Electrochem. Sci.*, 12 (2017) 9844.
47. H. Xu, H. Zhang, Y. Ouyang, L. Liu, Y. Wang, *Electrochim. Acta*, 214 (2016) 119.
48. H. Ru, K. Xiang, W. Zhou, Y. Zhu, X. S. Zhao, H. Chen, *Electrochim. Acta*, 222 (2016) 551.
49. T. M. Huggins, J. M. Whiteley, C. T. Love, K. Lee, S.-H. Lee, Z. J. Ren, J. C. Biffinger, *ACS Appl. Mater. Inter.*, 8 (2016) 26868.
50. D.-J. Ryu, R.-G. Oh, Y.-D. Seo, S.-Y. Oh, K.-S. Ryu, *Environ. Sci. Pollut. R.*, 22 (2015) 10405.
51. B. Campbell, R. Ionescu, Z. Favors, C. S. Ozkan, M. Ozkan, *Sci. Rep.*, 5 (2015)
52. X. Peng, J. Fu, C. Zhang, J. Tao, L. Sun, P. K. Chu, *Nanosci. Nanotech. Lett.*, 6 (2014) 68.